PERGAMON

International Journal of Heat and Mass Transfer 45 (2002) 3997–4010

International Journal of HEAT and MASS TRANSFER

www.elsevier.com/locate/ijhmt

A numerical study of steady flow and temperature fields within a melt spinning puddle

M. Bussmann [a], J. Mostaghimi [a,*], D.W. Kirk [b], J.W. Graydon [b]

[a] *Department of Mechanical and Industrial Engineering, University of Toronto, 5 King's College Road, Toronto, Ontario, Canada M5S 3G8*

[b] *Department of Chemical Engineering and Applied Chemistry, University of Toronto, Toronto, Canada M5S 3G8*

Received 19 February 2001; received in revised form 29 January 2002

Abstract

A numerical solution of the momentum and energy equations yields steady flow and temperature fields within a melt spinning puddle. The model accounts for inertial, viscous, surface tension, and wetting effects, and relies on a temperature-dependent viscosity to solidify ribbon to an amorphous state. A reference simulation is presented, followed by results that examine the effect of varying individual parameters. Results demonstrate a strong influence of nozzle wetting on puddle size; significant recirculation upstream of the nozzle slot; and the presence of both recirculation and an unrelated bump downstream of the slot. © 2002 Elsevier Science Ltd. All rights reserved.

1. Introduction

Planar flow casting, or melt spinning, is a process used to produce rapidly solidified material as ribbon or foil. Fig. 1 illustrates the process. In general terms, molten material is ejected from a crucible through a narrow rectangular nozzle onto a cold rotating wheel. The nozzle is positioned just above the wheel, so that at start-up molten material floods the gap between the underside of the nozzle and the top of the wheel, forming a steady state pool, or puddle. The rotating wheel cools and solidifies material, and at steady state, pulls solid ribbon out from beneath the puddle at the rate at which molten material is being injected.

The process has gained wide acceptance as a means of producing amorphous metallic materials for a variety of applications. Our interest is motivated by the use of amorphous Ni-base alloys as electrocatalysts in the hydrogen evolution reaction [1,2]. Amorphous alloys can sustain greater electrocatalytic activity than their crystalline counterparts and are more corrosion resistant. And when the apparatus is successfully producing ribbon, the melt spinning process offers a simple means of quickly generating a final product from the melt.

It is the successful and repeatable production of ribbon, however, that often presents an obstacle to utilizing melt spinning as a production process. A recent review of the fluid mechanics of melt spinning [3] focused much attention on issues of stability. An unstable process can reduce the rate of heat transfer from the melt, and thus yield a crystalline rather than an amorphous material. Various surface features of a ribbon are indications of a flow instability. At worst, a steady puddle fails to form at all, and the process yields a spray of material rather than a ribbon. Tuning the process is difficult because it depends on a large number of factors, including material composition and properties, melt temperature and pressure, geometric factors, wheel speed, the quality of the wheel surface, and the presence of a gas phase about the puddle. Our own experience with melt spinning has occasionally proved frustrating. Spinning some new alloy composition usually demands a significant investment of time to find the operating conditions that will produce a successful run of ribbon.

This experience led us to develop the model presented here. While there are certainly other models of the

* Corresponding author. Tel.: +1-416-978-5604; fax: +1-416-978-7753.

E-mail address: mostag@mie.utoronto.ca (J. Mostaghimi).

0017-9310/02/$ - see front matter
PII: S0017-9310(02)00112-6

Nomenclature

B	slot breadth
f	volume fraction
$\vec{F}_{ST}$	volumetric surface tension force
$\vec{g}$	gravity
G	gap height
h	heat transfer coefficient
H	ribbon thickness
k	thermal conductivity
$\hat{n}$	unit normal vector
p	pressure
Q	inlet flow rate per unit area
Re	Reynolds number ($\equiv \rho UH/\mu(T_0)$)
S	free surface area
t	time
Δt	timestep
T	temperature
T_{int}	ribbon/wheel interface temperature
T_0	initial melt temperature
T_{sol}	solid temperature
T_∞	ambient temperature
u, v	velocity components
U	wheel speed
$\vec{V}$	velocity
We	Weber number ($\equiv \rho U^2 H/\sigma$)
$\vec{x}$, $\vec{y}$	position vectors
Δx_i, Δy_j	cell dimensions

Greek symbols

α	thermal diffusivity
δ	Dirac delta function
ϵ	convolution radius
κ	curvature
μ	dynamic viscosity
θ	contact angle
ρ	density
σ	surface tension
$\tilde{\tau}$	viscous stress tensor

Subscripts

i, j	cell coordinates
in	nozzle slot
noz	nozzle underside
s	free surface
w	wheel

Superscripts

$'$	interim
$\tilde{}$	convolved
n, $n+1$	time levels
T	transpose

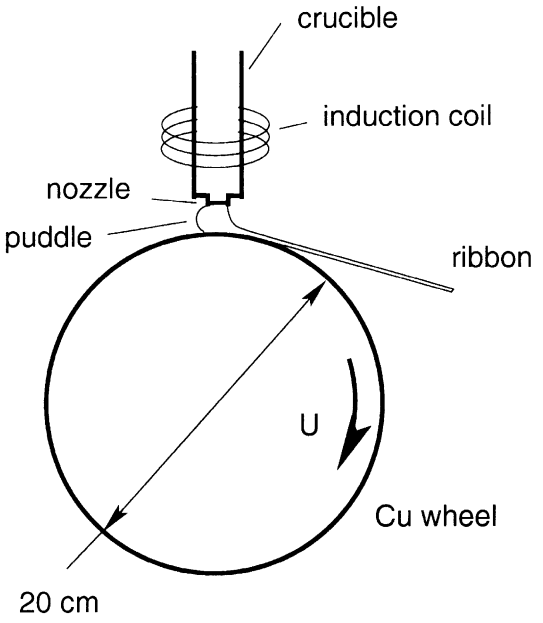

Fig. 1. Schematic of the melt spinner (not to scale).

process, including numerical ones, we are aware of few that represent a complete solution of the momentum and energy equations, and none that yield well-resolved results. In this paper, we present a model and various results that illustrate the effect of changes to various parameters on the flow and temperatures fields within a puddle. This paper focuses on steady solutions, and so does not explicitly address the issue of stability. Rather, we intend for this model and these results to serve as the basis for a subsequent study of the stability of the process.

We turn now to a brief summary of other models of puddle flow and temperature fields, and begin with the simplified integral analyses of Berger and Ai [4] and Steen et al. [5] that consider overall balances for mass, momentum, and energy within the puddle. The analyses do not provide detailed information about flow and temperature fields, but do yield important relationships between ribbon thickness and various operating parameters including applied pressure, nozzle geometry, wheel speed, and either melt and wheel temperatures [4] or a solidification rate [5]. Of note, both papers considered the extent of wetting between the melt and the underside of the nozzle, which has received little attention in subsequent studies.

More sophisticated analyses quickly turn to two-dimensional (2D) numerical studies, invoking various assumptions to simplify the computations. Gutierrez and Szekely [6] studied the puddle downstream of the nozzle, solving a set of equations based on lubrication

theory, coupled to an energy equation that accounted for phase change, and an empirical equation for downstream meniscus shape as a function of solidified thickness and operating parameters. Of note is the prediction of a recirculation zone in the downstream puddle above the ribbon. Gong et al. [7] made less assumptions by solving the boundary layer equations for flow, heat transfer, and phase change within the downstream portion of a puddle, examining the influence of various process parameters on the resulting puddle dynamics. The authors ignored surface tension along the downstream meniscus, and defined downstream detachment as the point of boundary layer separation. The authors went on to compare their numerical results to video images of actual puddle profiles, by varying the heat transfer coefficient until the calculated position of the downstream detachment point matched that observed experimentally. Wang and Matthys [8,9] subsequently extended the model of Gong et al. [7], implementing an improved solid/liquid interface tracking algorithm, while pointing out that the boundary layer equations were ill-suited to modeling the downward flow out of the nozzle and the flow near the detachment point. The authors used the model to focus on the heat transfer and solidification behaviour of a pure material, first for equilibrium solidification [8], and then allowing for undercooling and recalescence [9].

While the aforementioned models invoke various simplifications of the flow equations, and solved for flow only downstream of the nozzle, there are a series of studies that have attempted to solve the complete steady problem, including inertial, viscous, surface tension and wetting effects as well as solving for (rather than prescribing) the puddle menisci locations (using "volume-of-fluid" or VOF, codes). Many of the results, however, are based on very coarse mesh calculations, from which little quantitative information can be gleaned. Takeshita and Shingu [10] utilized SOLA-VOF [11], a 2D free surface flow code, to solve strictly for flow on a mesh of 40×10 cells. Wu et al. [12] added an energy equation and a temperature-dependent viscosity to SOLA-VOF, but again underresolved the puddle, with the ribbon thickness less than the height of a single cell. Chen and Hwang [13,14] presented similar calculations again at similar resolutions, both in two dimensions [13] and in three [14].

The only other numerical results of note are the better-resolved 2D calculations of Korzekwa et al. [15] and Thoma et al. [16], using FLOW-3D, a commercial VOF code that includes heat transfer and phase change capabilities. Of note is that simulations were run with an applied nozzle pressure rather than a prescribed inflow rate, and that the numerical solutions never reached a steady state, but rather fluctuated. The authors used measures of these fluctuations as an indication of stability, and found a reasonable correlation between this numerical stability and their ability to successfully spin actual ribbons.

This is clearly a brief overview of previous work. For a more complete review of the fluid mechanics of melt spinning, see the excellent review article by Steen and Karcher [3]. It seems fair to say that although much has been learned by way of modeling, there is room for another model, and in particular a numerical treatment of a complete set of equations applied to the entire puddle, with results calculated on sufficiently fine meshes to capture some of the details of the flow and temperature fields. This is our intent here. We consider the melt spinning of an amorphous material, from the initial impact of fluid onto the wheel through to the formation of a steady state puddle and the generation of ribbon of uniform thickness. The model incorporates the essential physics, including inertial, viscous, surface tension, and wetting effects, and relies on a temperature-dependent viscosity to solidify the ribbon. The equations are solved throughout the puddle, from the upstream meniscus to the downstream emergence of ribbon. Of interest are the flow and temperature fields within the puddle, and the manner in which these fields respond to changes in various operating parameters. In the remainder of the paper, we detail the equations and numerical methodology, briefly demonstrate some validation results, describe a reference simulation corresponding to experimental conditions that have proved successful in our laboratory, and finally present the results of a series of other simulations that consider the effect of changing reference operating conditions one at a time.

2. Methodology

2.1. Equations

We formulate the model based on the following assumptions:

- since ribbon width is much larger than the gap height G, the puddle is essentially 2D
- since the wheel diameter is much larger than the puddle length, wheel curvature beneath the puddle is negligible, and the bottom of the puddle is assumed to be flat
- melt inflow rate Q is constant; this frees the model of solving for flow within the crucible and nozzle that are much larger than the puddle, at the expense of not applying crucible pressure as a boundary condition
- the melt is incompressible and Newtonian, and puddle flow is laminar
- melt density ρ, surface tension σ, and thermal diffusivity α are constant; dynamic viscosity μ varies with temperature

- spinning occurs within a vacuum chamber, so that viscous stresses at the free surface are zero, and the only fluid flow is within the melt
- the ribbon cools to an amorphous state, which implies that the cooling rate is on the order of 10^6 (K/s)
- the wheel is the sole heat sink, and contact between ribbon and wheel is characterized by a single value of a heat transfer coefficient h
- the wheel temperature remains constant; while studies have demonstrated that wheel temperature increases at start-up, we are concerned with steady state behaviour
- the nozzle is adiabatic and radiative heat transfer from the puddle is negligible

The third assumption requires some elaboration. In practice, one applies a crucible pressure that drives fluid through the nozzle. The subsequent flow rate, and corresponding ribbon thickness, are then a function of the applied pressure, rather than a parameter that an operator can set. We, like others [6–10,12–14], however, chose to consider the steady problem offered by imposing a fixed inflow rate. This tends to simplify the numerics, but at the expense of imposing a stability on the flow that may not exist in practice.

The resulting problem is strictly one of fluid flow and heat transfer, with solidification resulting from the increase in viscosity associated with the cooling of the melt. The equations for conservation of mass, momentum, and energy in the melt phase are

$$\nabla \cdot \vec{V} = 0 \tag{1}$$

$$\frac{\partial \vec{V}}{\partial t} + \nabla \cdot (\vec{V}\vec{V}) = -\frac{1}{\rho}\nabla p + \frac{1}{\rho}\nabla \cdot \tilde{\tau} + \vec{g} + \frac{1}{\rho}\vec{F}_{\mathrm{ST}} \tag{2}$$

$$\frac{\partial T}{\partial t} + \nabla \cdot (\vec{V}T) = \alpha \nabla^2 T \tag{3}$$

Since the melt is Newtonian, the shear stress tensor $\tilde{\tau}$ may be written

$$\tilde{\tau} = \mu(\nabla \vec{V} + (\nabla \vec{V})^{\mathrm{T}}) \tag{4}$$

The viscosity varies with temperature. We assume it to be of the Vogel–Fulcher form [17] commonly used to describe the viscosity variation of amorphous materials through the glass transition

$$\mu = \mu_0 \exp\left(\frac{A}{T - C}\right) \tag{5}$$

μ_0, A and C are material-specific constants. Surface tension $\vec{F}_{\mathrm{ST}}$ is modeled as a volume force acting on fluid near the puddle-free surface, as originally formulated by Brackbill et al. [18]

$$\vec{F}_{\mathrm{ST}}(\vec{x}) = \sigma \int_S \kappa(\vec{y})\hat{n}_{\mathrm{s}}(\vec{y})\delta(\vec{x} - \vec{y})\,\mathrm{d}S \tag{6}$$

$\hat{n}_{\mathrm{s}}$ represents the unit normal to the free surface directed into the fluid, $\vec{y}$ is a position vector to points on the free surface, $\kappa = -\nabla \cdot \hat{n}_{\mathrm{s}}$ is the curvature of the free surface, δ is the Dirac delta function, and the integration is performed over the free surface S.

In addition to the flow equations, the model includes an algorithm to track the location of the puddle menisci. The approach chosen is a volume tracking technique; we define a scalar function f as

$$f = \begin{cases} 1 & \text{within the melt} \\ 0 & \text{without} \end{cases} \tag{7}$$

Since f is passively advected with the flow, it satisfies the advection equation

$$\frac{\partial f}{\partial t} + (\vec{V} \cdot \nabla) f = 0 \tag{8}$$

Boundary conditions are applied at the solid underside of the nozzle, at the nozzle slot, at the wheel, and at the puddle-free surface; we denote these boundaries by subscripts noz, in, w and s respectively.

At solid surfaces, no-penetration and no-slip conditions apply. At the wheel, this implies that fluid moves with the wheel speed U. At the puddle-free surface, the boundary condition on velocity is the zero stress condition, $\tilde{\tau}_{\mathrm{s}} = 0$, and since surface tension has been included in Eq. (2), the boundary condition on pressure reduces to $p_{\mathrm{s}} = 0$. Evaluation of Eq. (6) requires that $\hat{n}_{\mathrm{s}}$ be defined at the triple points along the nozzle and wheel, where the solid, fluid and vacuum meet. We impose a contact angle θ at these points, as shown in Fig. 2. θ_{w}, at the upstream meniscus, will be an advancing dynamic contact angle; at steady state, the two θ_{noz} will be static angles. Although dynamic contact angles are a function of contact line velocity, we assign constant values to all angles, for lack of data. At the nozzle slot, we impose a parabolic velocity profile corresponding to the melt flow rate Q, and a zero gradient condition on pressure, to reflect what will in reality be a small change in pressure relative to pressure variations within the puddle. The melt flowing into the gap is assigned the initial melt temperature T_0, and the temperature gradient

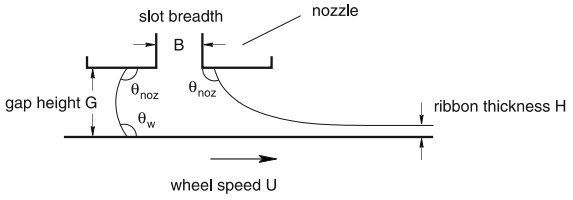

Fig. 2. Closeup of the puddle.

within the melt at the wheel is defined via a heat transfer coefficient h

$$k\nabla T\cdot\hat{\boldsymbol{n}}_{\mathrm{w}}=h(T_{\mathrm{int}}-T_{\infty}) \tag{9}$$

k is the thermal conductivity of the melt, and T_{int} and T_{∞} are the ribbon/wheel interface temperature and the ambient temperature, respectively.

As for initial conditions, since the process begins with an empty gap, the boundary conditions at the nozzle slot also serve as the initial conditions for the model.

2.2. Numerical formulation

The basis for our model is RIPPLE [19], a 2D fixed-grid Eulerian code written specifically for free surface flows with surface tension. Significant improvements have been incorporated into RIPPLE, including new surface tension and interface tracking algorithms, and a temperature-dependent dynamic viscosity. What follows is an overview of the numerical formulation, focusing on the improvements.

Eqs. (1)–(6) are discretized according to typical finite volume conventions on a rectilinear grid, illustrated in Fig. 3(a), that extends upwards from the wheel surface to the nozzle underside. The left edge of the grid extends beyond the upstream end of the puddle; the right edge is located sufficiently far downstream that the fluid exiting the grid can be considered solid ribbon. Velocities are specified at the centre of cell faces, and pressure and temperature at each cell centre, illustrated in Fig. 3(b).

2.2.1. Interface tracking

To discretize f we define a *volume fraction* $f_{i,j}$ that represents the fraction of the volume of cell (i,j) occupied by fluid

$$f_{i,j}=\frac{1}{\Delta x_i\,\Delta y_j}\int_{\Delta x_i}\int_{\Delta y_j} f\,\mathrm{d}y\,\mathrm{d}x \tag{10}$$

Cells filled with fluid are characterized by $f_{i,j}=1$, empty cells by $f_{i,j}=0$, and cells that define a portion of the interface by $0<f_{i,j}<1$, deemed "interface cells". To illustrate, Fig. 4(b) portrays the volume fractions corresponding to the exact (albeit unknown) interface of Fig. 4(a).

The model incorporates the interface advection algorithm of Youngs [20] to solve Eq. (8) geometrically. At each timestep, the algorithm consists of two steps. First, the free surface is reconstructed by locating a plane within each interface cell corresponding to $f_{i,j}$ and an estimate of the orientation of the interface $\hat{\boldsymbol{n}}_{i,j}$. The reconstructed interface is depicted in Fig. 4(b); note that the algorithm does not require that interface planes be contiguous. The second step is a geometric evaluation of volume fluxes using the latest cell face velocities, to obtain an updated volume fraction field. Fig. 4(c) illustrates the calculation of a volume flux across one face of a cell.

2.2.2. The pressure/velocity/temperature solution

A temporal discretization of Eq. (2) yields the basis for a two-step projection method

$$\frac{\vec{V}'-\vec{V}^n}{\Delta t}=-\nabla\cdot(\vec{V}\vec{V})^n+\frac{1}{\rho^n}\nabla\cdot\tilde{\tau}^n+\vec{g}^n+\frac{1}{\rho^n}\vec{F}^n_{\mathrm{ST}} \tag{11}$$

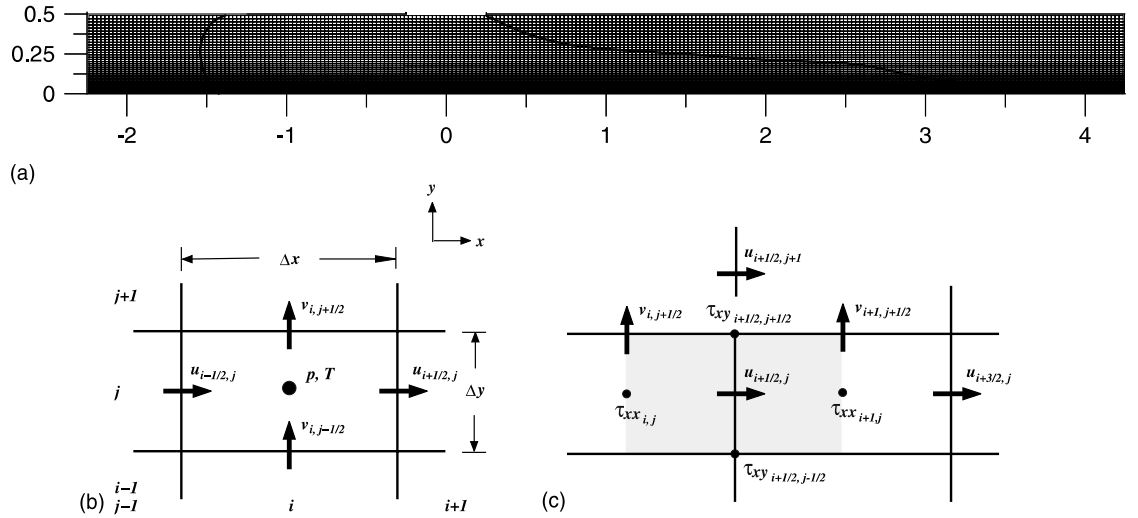

Fig. 3. (a) An example of the numerical grid (260×40 cells) with a puddle superimposed; (b) an individual cell (i,j), with velocities u and v specified at the cell faces, pressure p and temperature T at the cell centre; (c) a staggered x-momentum control volume centred at $(i+1/2,j)$, with shear stresses specified at cell faces.

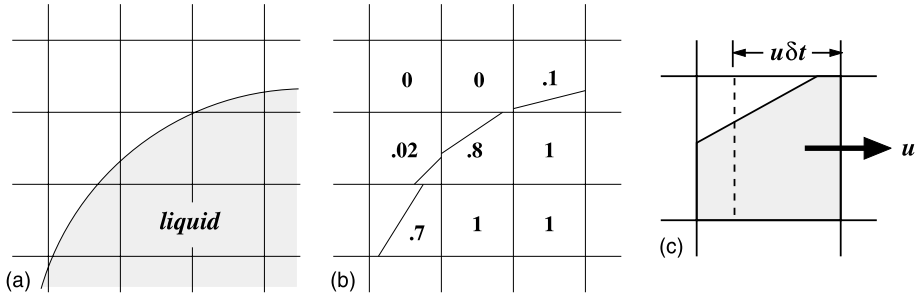

Fig. 4. The interface tracking method. (a) An exact liquid interface. (b) The corresponding volume fractions and planar interfaces. (c) With velocity u positive, the shaded region to the right of the dotted line is advected into the neighbouring cell during the timestep δt.

$$\frac{\vec{V}^{n+1}-\vec{V}'}{\Delta t}=-\frac{1}{\rho^n}\nabla p^{n+1} \tag{12}$$

In the first step, Eq. (11), an interim velocity $\vec{V}'$ is computed explicitly from convective, viscous, gravitational and surface tension accelerations of the known field $\vec{V}^n$ for a timestep Δt. In the second step, $\vec{V}'$ is projected onto a divergence-free velocity field: combining Eq. (12) with Eq. (1) at the new time level $(n+1)$ yields a Poisson equation for pressure

$$\nabla\cdot\left(\frac{1}{\rho^n}\nabla p^{n+1}\right)=\frac{1}{\Delta t}\nabla\cdot\vec{V}' \tag{13}$$

Although the fluid is assumed incompressible, the density is retained within the divergence operator to account for non-zero density gradients at the puddle-free surface. At solid surfaces, we impose a zero gradient condition on pressure

$$\nabla p\cdot\hat{\boldsymbol{n}}_{\mathrm{noz}}=\nabla p\cdot\hat{\boldsymbol{n}}_{\mathrm{w}}=0 \tag{14}$$

as a numerical means of enforcing the zero velocity condition. The resulting set of linear equations in p^{n+1} is symmetric and positive definite; a solution is obtained at each timestep with an incomplete Cholesky conjugate gradient (ICCG) solver. The new velocity field $\vec{V}^{n+1}$ is then evaluated via Eq. (12).

For control volume faces between two cells containing fluid, the convective term is discretized according to the method of van Leer [21]. Beginning with a second order central difference approximation for the fluxed momentum, the method introduces just enough upwinding to guarantee stability. At faces adjacent to a free surface, where one cannot construct a second-order approximation, momentum fluxes are approximated by upwind values.

Shear stresses are evaluated via a central differencing scheme at the staggered cell faces, as illustrated in Fig. 3(c). Viscosities associated with the shear stresses are a function of the local temperature: τ_{xx} and τ_{yy} are cell-centred quantities, and thus a function of the cell-centred temperature; τ_{xy} are located at cell vertices, where the viscosity is evaluated as a harmonic mean of the four surrounding viscosities.

Surface tension is treated in the following manner. To begin, a discrete surface tension force $\vec{F}_{\mathrm{ST}_{i,j}}$ is evaluated for each interface cell

$$\vec{F}_{\mathrm{ST}_{i,j}}=\sigma\kappa_{i,j}\frac{S_{i,j}}{\Delta x_{i,j}\,\Delta y_{i,j}}\hat{\boldsymbol{n}}_{s,i,j} \tag{15}$$

$S_{i,j}$ represents the interface area contained within the cell, evaluated as a byproduct of the interface advection algorithm. A finite kernel δ_ϵ, acting over a radius ϵ, is then introduced to approximate δ. The $\vec{F}_{\mathrm{ST}_{i,j}}$ are convolved over the radius ϵ to yield a force field $\vec{\tilde{F}}_{\mathrm{ST}_{i,j}}$ diffused over cells in the vicinity of the free surface

$$\vec{\tilde{F}}_{i,j}=2f_{i,j}\sum_{m,n}\vec{F}_{\mathrm{ST}_{m,n}}\delta_\epsilon(\vec{x}_{i,j}-\vec{y}_{m,n})\Delta x_m\,\Delta y_n \tag{16}$$

Note that the $2f_{i,j}$ in front of the summation serves as a weighting function to transform the volumetric force into a body force acting only on cells that contain fluid.

Estimates of $\hat{\boldsymbol{n}}_{i,j}$ and $\kappa_{i,j}$, which are geometric characteristics of the interface, are obtained from the volume fractions

$$\hat{\boldsymbol{n}}=\frac{\vec{\nabla}f}{|\vec{\nabla}f|}\quad \kappa=-\vec{\nabla}\cdot\hat{\boldsymbol{n}} \tag{17}$$

Because the $f_{i,j}$ are discontinuous, estimates of $\vec{\nabla}f$ are obtained by evaluating the gradient of a convolved $f_{i,j}$ field. We employ the same kernel δ_ϵ to convolve $f_{i,j}$ as $\vec{F}_{\mathrm{ST}_{i,j}}$

$$\delta_\epsilon(\vec{x})=\begin{cases}\left(1+\cos\left(\frac{\pi|\vec{x}|}{\epsilon}\right)\right)/c & |\vec{x}|\leqslant\epsilon\\ 0 & |\vec{x}|>\epsilon\end{cases} \tag{18}$$

where c normalizes the kernel

$$c=\epsilon^2(\pi^2-4)/\pi \tag{19}$$

It should be noted that this method of evaluating $\hat{\boldsymbol{n}}$ is different than that proposed by Youngs [20]. We do, however, incorporate all other aspects of Youngs' interface advection algorithm.

Following the solution of the flow equations at each timestep, Eq. (3) is solved for a new temperature field T^{n+1}. The convective and diffusive terms are treated explicitly in a manner similar to that of the flow equations, but with a thermal diffusivity that is not a function of temperature.

2.2.3. Timestep restrictions

The explicit evaluation of the convective, viscous, surface tension, and thermal diffusion terms places the following restrictions on the magnitude of the allowable timestep, in order to maintain the stability of the solution

$$\max\left[\frac{|u_{i,j}|\,\Delta t}{\Delta x_i},\frac{|v_{i,j}|\,\Delta t}{\Delta y_j}\right] < 1 \tag{20}$$

$$\Delta t < \frac{\rho}{\mu}\cdot\frac{(\Delta x_i)^2(\Delta y_j)^2}{(\Delta x_i)^2+(\Delta y_j)^2} \tag{21}$$

$$\Delta t < \sqrt{\frac{\rho}{4\pi\sigma}}\cdot\min\left[(\Delta x_i)^{3/2},(\Delta y_j)^{3/2}\right] \tag{22}$$

$$\Delta t < \frac{1}{\alpha}\cdot\frac{(\Delta x_i)^2(\Delta y_j)^2}{(\Delta x_i)^2+(\Delta y_j)^2} \tag{23}$$

The viscous restriction is by far the most stringent of these, because as the melt cools, the viscosity increases exponentially, and the timestep becomes very small. While an implicit treatment of the viscous term would remove this restriction, such an implementation would substantially increase the complexity of the flow algorithm. While we are pursuing such an approach for future work, we devised the following alternative within the framework of the methodology presented here.

2.2.4. Flow in "solid ribbon"

As the melt cools, the fluid velocity rapidly approaches U, as one would expect. And although there is no explicit interface between liquid and solid material, there certainly is a temperature below which there is little point to solving the flow equations. This led us to incorporate a filter into the algorithm, to flag those cells that had dropped below some solid temperature T_{sol}, to remove them from the flow solution domain, and instead impose upon them the wheel speed U. T_{sol} was evaluated by running simulations without the filter, and examining the relationship between velocity and temperature. For all of the simulations presented here, a fluid velocity was within one percent of U prior to a cell being flagged.

3. Results and discussion

The parameters associated with a series of simulations are summarized in Table 1. We begin this discussion by considering a reference problem, then briefly present results of a validation study, and finally examine a series of simulations that consider the influence of various parameters on the flow and temperature fields within a melt spinning puddle.

Table 2 presents material properties that we consider representative of a Ni–B alloy that we have spun in our laboratory. For lack of other data, the constant properties are the melting point values of pure Ni. The constants in the viscosity relationship were chosen to yield a reasonable value of viscosity (4×10^{-3} Pa s) at the melting point ($\approx$1400 K) of our alloy.

The reference problem corresponds to operating parameters that we have used to successfully spin Ni–B ribbon, and are listed in the first row of Table 1. The grid geometry is defined by a gap height $G = 0.5$ mm, a slot breadth $B = 0.5$ mm, and a nozzle underside that extends 2 mm on other side of the slot. The heat transfer coefficient h is an unknown; our value of $h = 10^6$ W/m^2 K is based on suggestions in the literature (e.g. [7,22–24]). The value is on the high end of reported values, which we consider appropriate for the case of a melt cooling to an amorphous state in an ambient vacuum. On the underside of the nozzle, we prescribed a very non-wetting contact angle $\theta_{\mathrm{noz}} = 170°$ (see Fig. 2), based on experimental observations of nearly spherical solid melt that remained attached to the underside of the nozzle after the apparatus had cooled. The wheel contact angle at the upstream end of the puddle was set to $\theta_{\mathrm{w}} = 90°$ (see Fig. 2); while this value is arbitrary, we will show that it hardly matters, because the contribution of capillary forces at the wheel surface is small relative to viscous and inertial ones.

We ran a series of validation simulations of the reference problem (Table 1) to assess the influence of grid resolution and the value of T_{sol}. The plots of Fig. 5(a) and (b) present total puddle volume and ribbon thickness versus time as a function of mesh resolution; Fig. 5(c) and (d) presents the same indicators as a function of T_{sol}. All of our tests demonstrated good convergence. The results are also indicative of a number of other measures that were plotted. Note that the total fluid volume increases linearly from $t = 0$ under a prescribed flow rate until cold fluid (ribbon) begins to exit the mesh at about 0.3 ms. Note too that while the curves of total fluid volume are smooth, the curves of ribbon thickness fluctuate somewhat. We only ran the validation simulations to 5 ms, before a steady state had been reached. Later simulations were run to steady state, with the elapsed time listed in the last column of Table 1. At steady state, the fluctuations in ribbon thickness had disappeared, with the volume of material exiting the grid equal to the prescribed flow rate. The validation provided the data required to assess grid independence: we ran all remaining simulations at a resolution of 40 cells in the y-direction by at least 220 cells, adding cells in the

Table 1
Summary of simulations

U (m/s)	Q (m/s)	T_0 (K)	h (W/m^2 K)	θ_{noz}	θ_w	T_{sol} (K)	H/G	Re	We	Resolution	Calc. time (ms)
Reference											
26	2.25	1500	1×10^6	170°	90°	950	0.087	3237	135	220×40	19.5
Validation											
26	2.25	1500	1×10^6	170°	90°	**940**	0.087	3237	135	165×30	5.0
26	2.25	1500	1×10^6	170°	90°	**960**	0.087	3237	135	165×30	5.0
26	2.25	1500	1×10^6	170°	90°	**970**	0.087	3237	135	165×30	5.0
26	2.25	1500	1×10^6	170°	90°	950	0.087	3237	135	$\mathbf{110 \times 20}$	25.0
26	2.25	1500	1×10^6	170°	90°	950	0.087	3237	135	$\mathbf{132 \times 24}$	15.0
26	2.25	1500	1×10^6	170°	90°	950	0.087	3237	135	$\mathbf{165 \times 30}$	20.0
26	2.25	1500	1×10^6	170°	90°	950	0.087	3237	135	$\mathbf{275 \times 50}$	5.0
Results											
13	2.25	1500	1×10^6	170°	90°	950	0.173	3237	68	260×40	9.25
39	2.25	1500	1×10^6	170°	90°	950	0.058	3237	203	220×40	20.0
26	**1.125**	1500	1×10^6	170°	90°	950	0.043	1618	68	220×40	8.5
26	**3.375**	1500	1×10^6	170°	90°	950	0.130	4855	203	260×40	12.75
26	2.25	**1400**	1×10^6	170°	90°	950	0.087	2141	135	220×40	14.6
26	2.25	**1600**	1×10^6	170°	90°	950	0.087	4453	135	240×40	23.85
26	2.25	1500	$\mathbf{1.5 \times 10^6}$	170°	90°	950	0.087	3237	135	220×40	14.0
26	2.25	1500	$\mathbf{0.5 \times 10^6}$	170°	90°	950	0.087	3237	135	260×40	13.85
26	2.25	1500	1×10^6	**10°**	90°	950	0.087	3237	135	240×40	1.35
26	2.25	1500	1×10^6	**90°**	90°	950	0.087	3237	135	240×40	25.0
26	2.25	1500	1×10^6	**130°**	90°	950	0.087	3237	135	220×40	35.0
26	2.25	1500	1×10^6	170°	**130°**	950	0.087	3237	135	220×40	20.0

The highlighted quantities indicate how the simulations differ from the reference simulation.

Table 2
Thermophysical properties of the Ni–B melt

$\rho = 7870$ kg/m^3
$\sigma = 1.7$ N/m
$\mu = 1.66 \times 10^{-4} \exp\left(\frac{2180}{T-722}\right)$ Pa s (T in K)
$k = 90$ W/m K
$\alpha = 2.6 \times 10^{-5}$ m^2/s

x-direction to accommodate longer puddles. The mesh was equally spaced in the x-direction, while cells in the y were focused near the wheel, as illustrated in Fig. 3(a). The temperature at which ribbon was deemed solid was specified as $T_{sol} = 950$ K.

We turn now to the results of the reference simulation. Fig. 6 illustrates the evolution of the puddle shape to 10.0 ms, when the profile has ostensibly reached steady state, although we ran the simulation to 19.5 ms. Fig. 7 illustrates the corresponding steady state streamlines and isotherms. Note that the plots of Fig. 7 and of many subsequent figures have been stretched four times in the vertical direction, to offer a clearer view of the flow and temperature fields within the puddle. Fig. 8 illustrates the pressure variation along the base of the puddle, relative to a zero ambient pressure.

We begin with a few observations regarding Fig. 6. Note first that the puddle shapes are qualitatively similar to the few photographs that have been published (e.g. [6,7,25–27]), and to the results of other numerical studies (e.g. [6–10,12,13]). While the upstream end of the puddle moves well away from the nozzle, the downstream end is pinned at the slot. The reason, as we will show, is related to the large value of θ_{noz} that we imposed, which reflects a large difference in solid surface energies on either side of the contact line. Note too that the convex puddle profile at the upstream end is not symmetric about the gap midline, even though it may appear so in the profile at 10.0 ms. The convexity is a direct result of the large value of θ_{noz} at the top of the gap, and of the wheel moving to the right at the bottom. Finally, note the presence of a subtle bump in the puddle profile downstream of the slot, which has been observed previously [6].

Fig. 7 clearly illustrates the presence of recirculation both up and downstream of the slot. The downstream recirculation has been seen before [6,10], and is thought to be related to the bump. We will say more about this in a moment. On the upstream side, there are two vortices rotating in different directions, driven by the downward flow out of the nozzle. The corresponding isotherms reflect this movement of fluid, as the 1450 and 1400 K

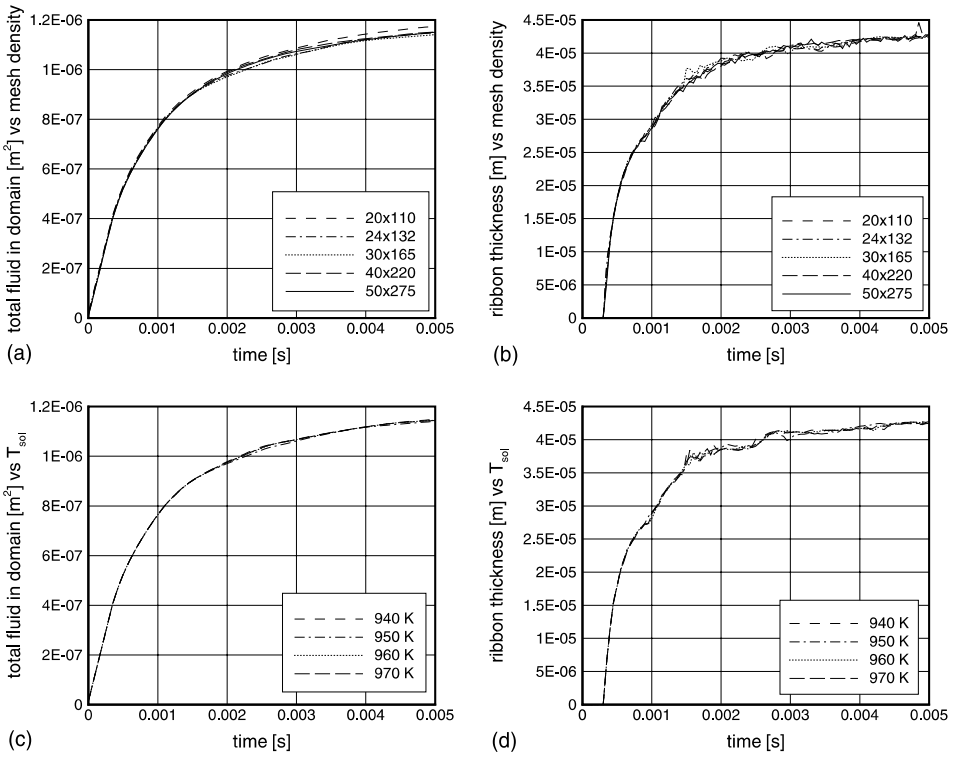

Fig. 5. The effect of mesh resolution on (a) total fluid volume and (b) ribbon thickness, and the effect of the value of T_{sol} on (c) total fluid volume and (d) ribbon thickness.

isotherms extend vertically all the way up to the nozzle. As a result, the fluid temperature at the upstream melt/wheel contact line is significantly lower than T_0, the initial melt temperature. Also important is that the streamlines reveal that a significant fraction of melt ejected from the nozzle flows upstream before being entrained by the rotation of the wheel. As a result, models of only the flow downstream of the nozzle (e.g. [6–9]) are simplifying the problem in a way that may not always be appropriate.

The pressure at the base of the puddle varies as one might expect: peak pressure is beneath the inlet, turning the flow onto the wheel. At the upstream meniscus, the non-zero pressure reflects the influence of surface tension across a highly curved interface. Along the downstream menisci, the pressure decreases more gradually to zero. The appearance of a minimum value appears related to the nature of the flow downstream of the inlet: fluid turns almost 90° before turning again towards the wheel where the ribbon emerges from the puddle.

Fig. 9 presents the results of simulations examining the effect of decreasing the nozzle contact angle θ_{noz} from the reference value of 170°. Of note is the movement of the downstream contact line away from the nozzle slot, with distance increasing as θ_{noz} decreases. The resulting downstream flowfield is characterized by a much larger recirculation region, and by a very flat downstream meniscus, with no sign of the bump visible in the profile of Fig. 7. Such a configuration, of a detachment point downstream of the nozzle slot, is how puddle geometry is typically portrayed, which suggests that $\theta_{noz} = 170°$ may be too high a value. On the other hand, the value was chosen independent of the results of the model, based on an experimental observation, and so we deemed it inappropriate to adjust the value. We also ran a simulation with $\theta_{noz} = 10°$, a very wetting condition in sharp contrast to our reference simulation. However, we stopped the simulation at 1.35 ms, because fluid was advancing quickly along the upstream underside of the nozzle, and would soon have reached the mesh boundary. The resulting concave meniscus appears very unrealistic. Fig. 10 portrays the results at the time the simulation was stopped.

To complete this discussion of wetting behaviour, we also ran a simulation for $\theta_w = 130°$. Unlike the influence of θ_{noz}, however, the results of this simulation were nearly indistinguishable from the reference results. It is clear that capillary forces are small relative to inertial and viscous ones at the wheel surface, in sharp contrast to the situation at the nozzle underside.

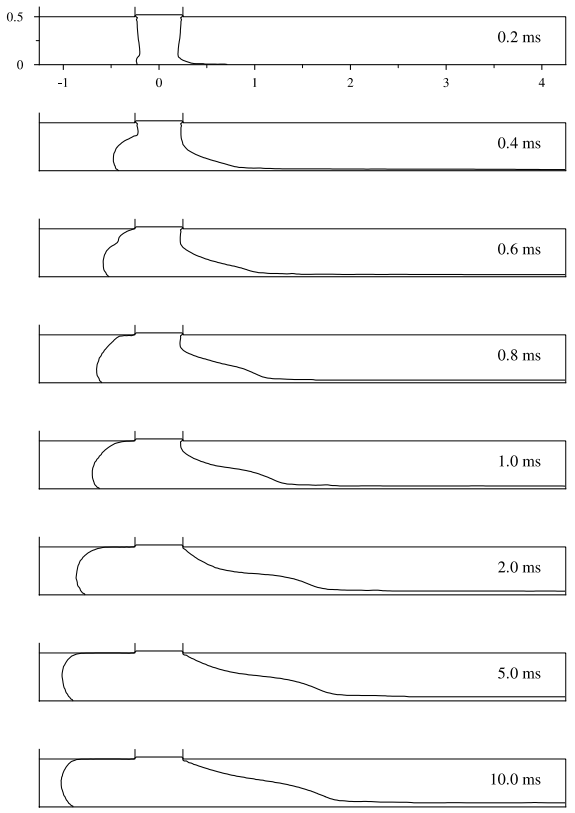

Fig. 6. Evolution of the puddle shape to a steady configuration—reference simulation.

Figs. 11–14 present results of simulations that consider the effect of varying wheel speed U, flow rate Q, inlet temperature T_0, and heat transfer coefficient h, respectively. For each of these variables, simulations were run for values both greater and less than the reference value. It is important to note that the parameter ranges are not all equivalent. While we vary T_0 by only 100 K on either side of 1500 K because we control this parameter experimentally, we investigate a range of h between 0.5 and 1.5×10^6 W/m^2 K because h is unknown, and the range of values quoted in the literature is very high. As a result, the plots of Fig. 14, for example, differ more than the plots of Fig. 13.

As one would expect, puddle length decreases as the characteristic cooling time decreases. Lower values of T_0

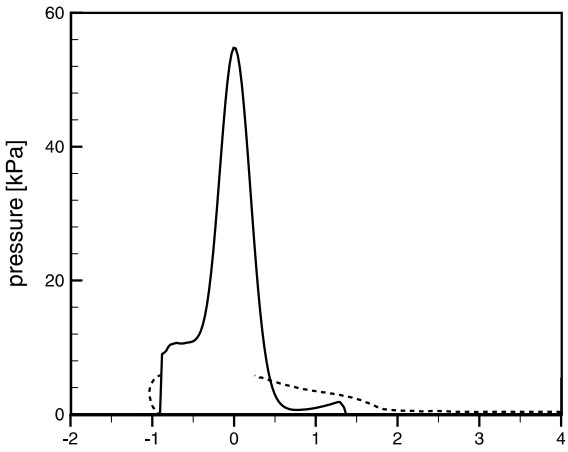

Fig. 8. Pressure variation along the base of the puddle, relative to a zero pressure outside the puddle. Note that the puddle profile (dashed) has been superimposed on the graph, for clarity.

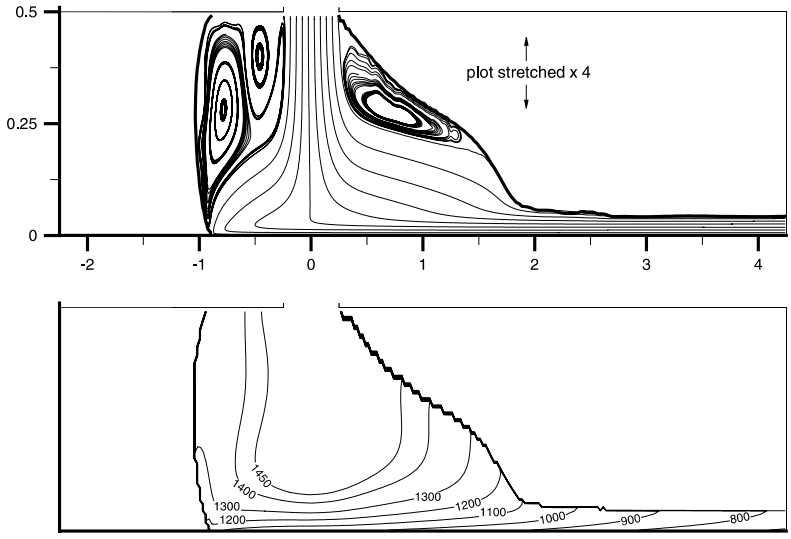

Fig. 7. Steady flow and temperature fields for the reference simulation. Note that this and many subsequent figures have been stretched in the vertical direction.

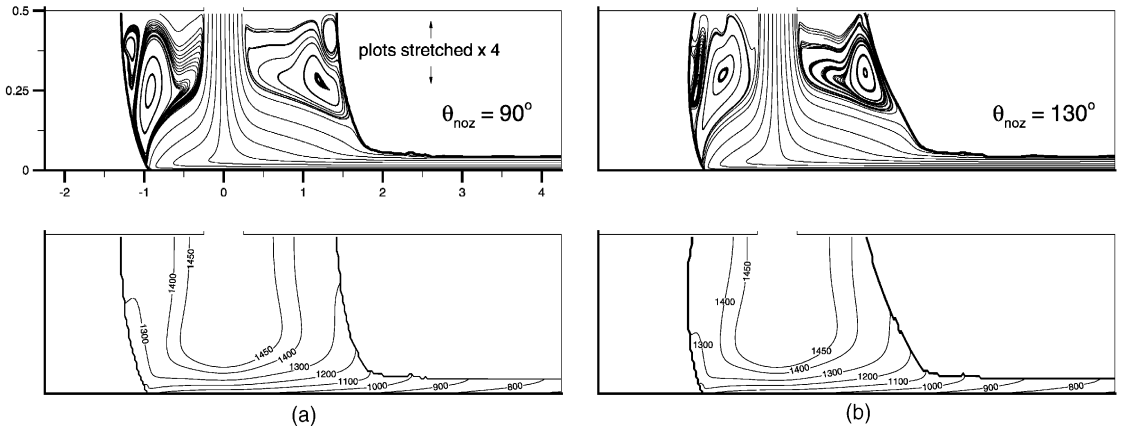

Fig. 9. Comparison of the flow and temperature fields for different values of the contact angle at the underside of the nozzle: (a) $\theta = 90°$ and (b) $\theta = 130°$.

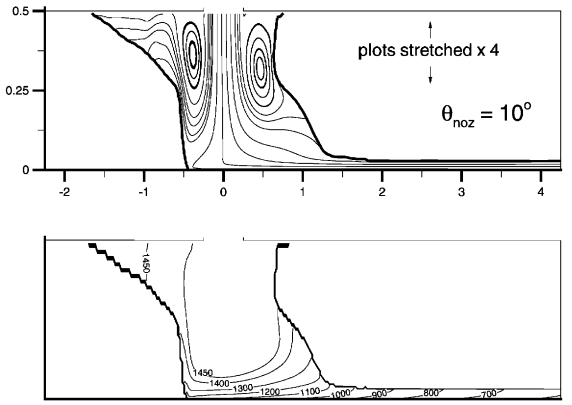

Fig. 10. Comparison of the flow and temperature fields for $\theta_{noz} = 10°$ at 1.35 ms.

and Q, that decrease the energy input into the puddle, and higher values of U and h that increase the cooling capacity, all lead to shorter puddles. And the flipside is true, that greater superheat and flow rate, slower wheel speed, and a lower value of h lead to longer puddles. The four figures also reveal that the number of upstream vortices increases with the length of the puddle upstream of the slot, while the downstream detachment point remains fixed at the downstream edge of the slot regardless of other puddle characteristics. Ribbon thickness H is not the same for each of these eight simulations, but rather varies as $H = QB/U$, and is listed in Table 1. As a result, the ribbons of Figs. 11 and 12 differ from the reference ribbon, and in retrospect, it appears that the mesh of Fig. 11(a) should have extended somewhat further downstream, as the temperature of the ribbon exiting the mesh is still above T_{sol}.

Turning to the downstream flowfields of Figs. 11–14, we note the presence of both vortices and bumps, but little correlation between them. The short puddles demonstrate more recirculation than the long ones, yet have very straight downstream menisci. In sharp

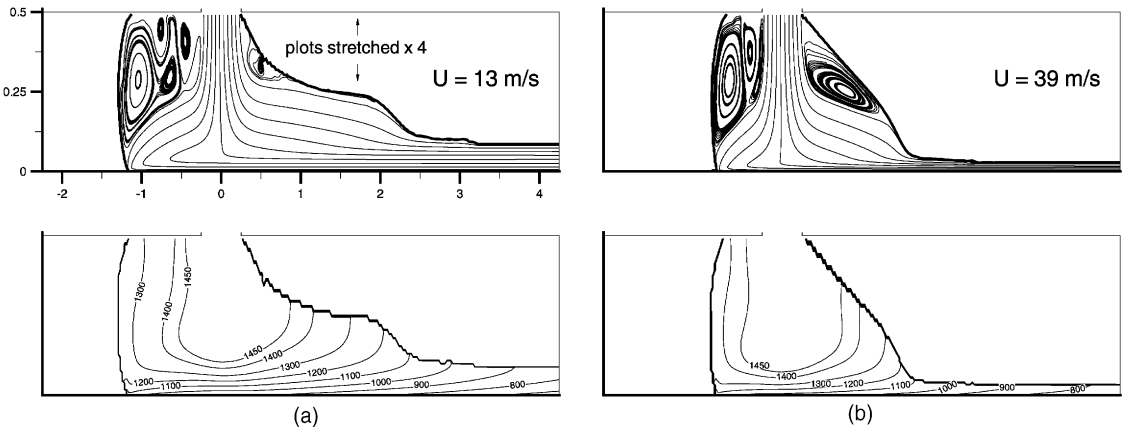

Fig. 11. Comparison of the flow and temperature fields for different values of the wheel speed: (a) $U = 13$ m/s and (b) $U = 39$ m/s.

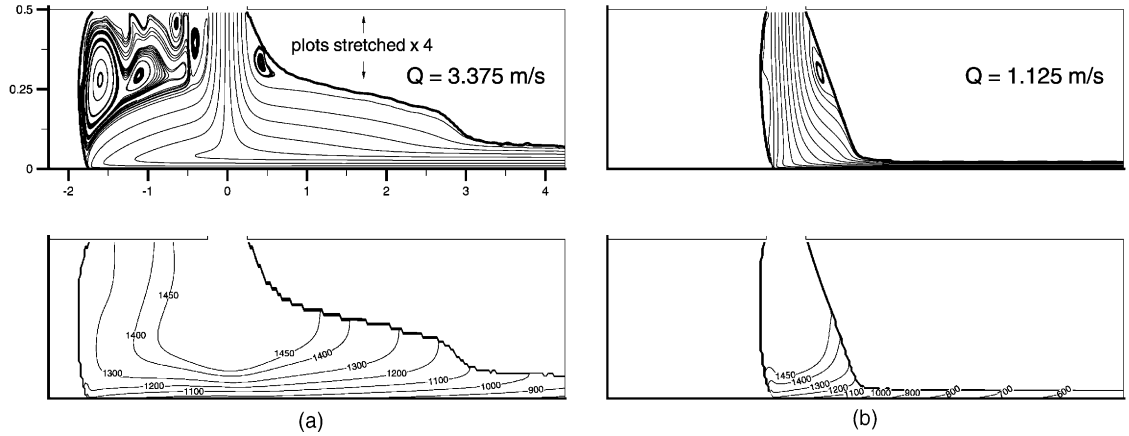

Fig. 12. Comparison of the flow and temperature fields for different values of the inlet flow rate: (a) $Q = 3.375$ m/s and (b) $Q = 1.125$ m/s.

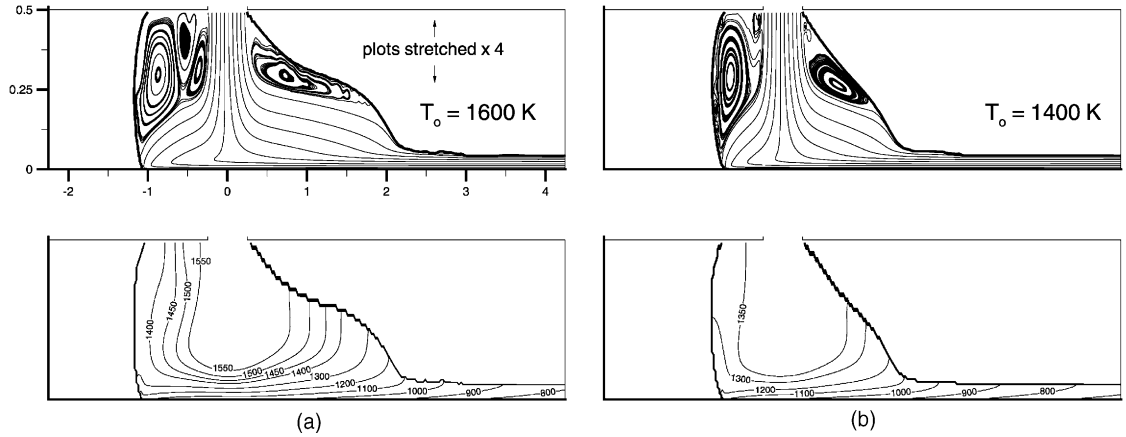

Fig. 13. Comparison of the flow and temperature fields for different values of the initial melt temperature: (a) $T_0 = 1600$ K and (b) $T_0 = 1400$ K.

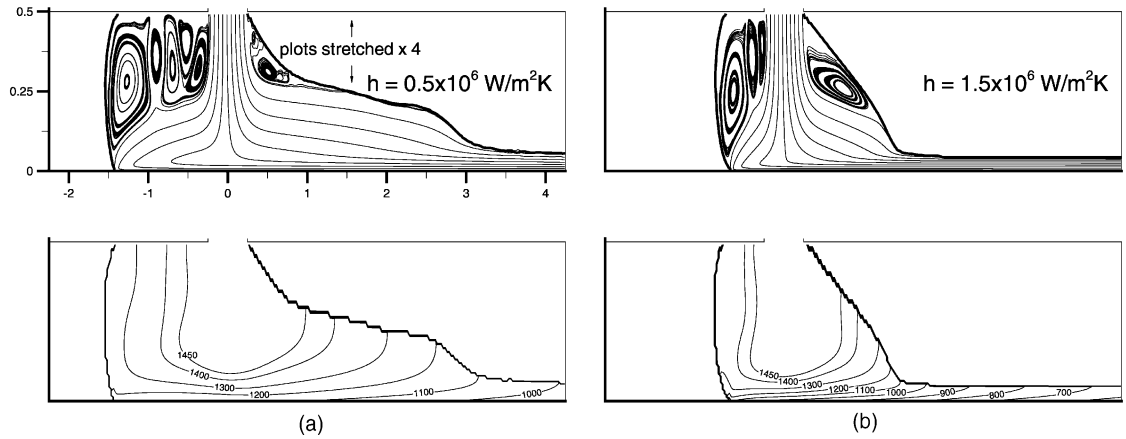

Fig. 14. Comparison of the flow and temperature fields for different values of the heat transfer coefficient: (a) $h = 0.5 \times 10^6$ W/m^2 K and (b) $h = 1.5 \times 10^6$ W/m^2 K.

contrast, the long puddles have noticeable bumps near the downstream end of the puddles, but only small vortices much nearer the nozzle slot. If one examines the isotherms within each of the four longer puddles, one can see the bump bounded by puddle surface temperatures of ≈1200 K at the top and 1100 K at the bottom. The corresponding change in viscosity is more than threefold.

The results suggest that for the system modeled here, that the ribbon is formed at about 1100 K, and that the flowfield above the ribbon is then defined by the downstream distance required to cool to that temperature. At shorter distances, the downstream meniscus is straight and recirculation is driven by a downward flow out of the slot. As the downstream distance to 1100 K increases, the flow out of the slot is allowed to turn more gradually, and thus tends not to drive a vortex. The bump then appears at whatever point the ribbon emerges from beneath the longer puddle.

4. Conclusions

We have considered the melt spinning of an amorphous material, presenting flow and temperature fields of a steady puddle. Results of a reference simulation are followed by a series of results corresponding to changes in individual operating parameters.

Results suggest the following:

- that the extent of wetting of the melt to the underside of the nozzle dramatically affects the position of the upstream and downstream detachment points, and thus the size of the puddle
- by contrast, wetting of the wheel at the upstream end of the puddle is insignificant relative to inertial and viscous effects
- flow within the puddle upstream of the slot is characterized by a series of vortices, with the extent of recirculation proportional to the upstream size of the puddle
- recirculation downstream of the slot appears only in shorter puddles, driven by a downward flow out of the slot; a characteristic bump that has been observed previously appears only at the far downstream end of longer puddles, and is related to the adjustment of the puddle flow to the emergence of ribbon from beneath the puddle

Acknowledgements

This work was made possible by the financial support of CHES, the Centre for Hydrogen and Electrochemical Studies at the University of Toronto.

References

[1] K. Lian, D.W. Kirk, S.J. Thorpe, Electrocatalytic behaviour of Ni-base amorphous alloys, Electrochim. Acta 36 (1991) 537–545.
[2] D.W. Kirk, S.J. Thorpe, H. Suzuki, Ni-base amorphous alloys as electrocatalysts for alkaline water electrolysis, Int. J. Hydrogen Energy 22 (1997) 493–500.
[3] P.H. Steen, C. Karcher, Fluid mechanics of spin casting of metals, Ann. Rev. Fluid Mech. 29 (1997) 373–397.
[4] S.A. Berger, D.K. Ai, A simple fluid mechanical model for planar flow casting melt-spinning, Metall. Trans. B 19 (1988) 571–579.
[5] P.H. Steen, J.K. Carpenter, H. Yu, Fluid mechanics of the planar-flow melt-spinning process, AIChE. J. 34 (1988) 1673–1682.
[6] E.M. Gutierrez, J. Szekely, A mathematical model of the planar flow melt spinning process, Metall. Trans. B 17 (1986) 695–703.
[7] Z. Gong, P. Wilde, E.F. Matthys, Numerical modelling of the planar flow melt-spinning process and experimental investigation of its solidification puddle dynamics, Int. J. Rapid Solidificat. 6 (1991) 1–28.
[8] G.-X. Wang, E.F. Matthys, An improved boundary-layer model for the planar flow melt-spinning process, in: E.F. Matthys, B. Kushner (Eds.), Advanced Sensing, Modelling, and Control of Materials Processing, TMS, Warrendale, PA, 1992, pp. 231–251.
[9] G.-X. Wang, E.F. Matthys, Two-dimensional boundary-layer modeling of planar flow melt-spinning with undercooling, in: E.F. Matthys (Ed.), Melt-spinning and Strip Casting: Research and Implementation, TMS, Warrendale, PA, 1992, pp. 263–282.
[10] K. Takeshita, P.H. Shingu, An analysis of the melt puddle formation in the single roller chill block casting, Trans. Jpn. Inst. Metals 27 (1986) 141–148.
[11] B.D. Nichols, C.W. Hirt, R.S. Hotchkiss, SOLA-VOF: A solution algorithm for transient fluid flow with multiple free boundaries, LASL report LA-8355, 1980.
[12] S.L. Wu, C.W. Chen, W.S. Hwang, C.C. Yang, Analysis for melt puddle in the planar flow casting process—A mathematical modelling study, Appl. Math. Modell. 16 (1992) 394–403.
[13] C.W. Chen, W.S. Hwang, A modified free surface treatment for the modeling of puddle formation in planar flow casting process, ISIJ Int. 35 (1995) 393–401.
[14] C.W. Chen, W.S. Hwang, A three-dimensional fluid flow model for puddle formation in the single-roll rapid solidification process, Appl. Math. Modell. 19 (1995) 704–712.
[15] D.R. Korzekwa, L.A. Jacobson, C.W. Hirt, Modeling planar flow casting with FLOW-3D, in: E.F. Matthys (Ed.), Melt-spinning and Strip Casting: Research and Implementation, TMS, Warrendale, PA, 1992, pp. 107–122.
[16] D.J. Thoma, E.M. Schwartz, S.R. Bingert, D.R. Korzekwa, R.D. Field, L.A. Jacobson, Microsegregation during melt-spinning of dilute palladium alloys, in: E.F. Matthys, W.G. Truckner (Eds.), Melt Spinning, Strip Casting and Slab Casting, TMS, Warrendale, PA, 1996, pp. 173–184.

[17] F. Yonezawa, Glass transition and relaxation of disordered structures, in: H. Ehrenreich, D. Turnbull (Eds.), Solid State Physics, Academic Press, Boston, 1991, pp. 179–254.
[18] J.U. Brackbill, D.B. Kothe, C. Zemach, A continuum method for modeling surface tension, J. Comput. Phys. 100 (1992) 335–354.
[19] D.B. Kothe, R.C. Mjolsness, RIPPLE: A new model for incompressible flows with free surfaces, AIAA J. 30 (1992) 2694–2700.
[20] D.L. Youngs, Time-dependent multi-material flow with large fluid distortion, in: K.W. Morton, M.J. Baines (Eds.), Numerical Methods for Fluid Dynamics, Academic Press, New York, 1982, pp. 273–285.
[21] B. van Leer, Towards the ultimate conservative finite difference scheme. V. A second-order sequel to Godunov's method, J. Comput. Phys. 32 (1979) 101–136.
[22] S.C. Huang, H.C. Fiedler, Effects of wheel surface conditions on the casting of amorphous metal ribbons, Metall. Trans. A 12 (1981) 1107–1112.
[23] A. Ludwig, G. Frommeyer, Investigations on the heat transfer during PFC-meltspinning by on line high speed temperature measurements, in: E.F. Matthys (Ed.), Melt-spinning and Strip Casting: Research and Implementation, TMS, Warrendale, PA, 1992, pp. 163–171.
[24] J. Kukura, K. Ford, A. Singh, P.H. Steen, T. Ibaraki, Measurement of heat transfer coefficient in planar flow casting, in: S.F. Shen, P.R. Dawson (Eds.), Simulation of Materials Processing: Theory, Methods and Applications, Balkema, Rotterdam, 1995, pp. 1153–1157.
[25] S.C. Huang, R.P. Laforce, A.M. Ritter, R.P. Goehner, Rapid solidification characteristics in melt spinning a Ni-base superalloy, Metall. Trans. A 16 (1985) 1773–1779.
[26] P.D. Wilde, E.F. Matthys, Experimental investigation of the planar flow casting process: development and free surface characteristics of the solidification puddle, Mater. Sci. Eng. A 150 (1992) 237–247.
[27] A.A. Tseng, Y. Sato, J.S. Chen, Modeling and monitoring of flow behavior of advanced materials in melt spinning: A progress report, in: E.F. Matthys, W.G. Truckner (Eds.), Melt Spinning, Strip Casting and Slab Casting, TMS, Warrendale, PA, 1996, pp. 195–204.